Advances in Geo-Energy Research

Vol. 19, No. 2, p. 166-181, 2026

Original article

Multi-scale characterizations of thermosensitive adhesive resin embedded with bridging materials: Toward forming stable plugging in fractured formations

Youming Lang[1], Yingrui Bai[1,2]*, Jinsheng Sun[1,2,3], Huazhou Li[4], Jingbin Yang[2], Kaihe Lv[1]

[1]*School of Petroleum Engineering, China University of Petroleum (East China), Qingdao 266580, P. R. China*

[2]*State Key Laboratory of Deep Oil and Gas, China University of Petroleum (East China), Qingdao 266580, P. R. China*

[3]*CNPC Engineering Technology R&D Company Limited, Beijing 102206, P. R. China*

[4]*School of Mining and Petroleum Engineering, Faculty of Engineering, University of Alberta, Edmonton T6G 1H9, Canada*

Keywords:
Thermosensitive adhesive resin
bridging material
interaction mechanism
discrete element simulation
fracture plugging
lost circulation control

Cited as:
Lang, Y., Bai, Y., Sun, J., Li, H., Yang, J., Lv, K. Multi-scale characterizations of thermosensitive adhesive resin embedded with bridging materials: Toward forming stable plugging in fractured formations. Advances in Geo-Energy Research, 2026, 19(2): 166-181.
https://doi.org/10.46690/ager.2026.02.05

Abstract:
Lost circulation in fractured formations remains a persistent challenge in drilling operations, causing substantial economic losses and increased operational risk. Conventional granular bridging packs are mechanically fragile and can be destabilized by pressure fluctuations, limiting one-trip plugging efficiency. This study incorporates a thermosensitive adhesive resin into bridging assemblies to enhance plug integrity by promoting interparticle adhesion and particle-wall coupling after thermal activation. Oscillatory temperature-sweep rheometry is used to quantify the temperature-dependent viscoelastic response of resin-particle composites. A wedge-shaped fracture analogue with photoelastic visualization is used to monitor force chain development and uniformity during progressive loading. Discrete element method simulations in Particle Flow Code, using a linear parallel-bond contact model, resolve mesoscale load-transfer pathways and isolate the contribution of adhesive interactions. Results indicate that thermosensitive adhesive resin increases assembly coherence, promotes a stable load-bearing skeleton, and suppresses stress localization that typically precedes plugging failure. The strengthening trend is governed by particle rigidity and surface characteristics, yielding consistent load-transfer patterns across experiments and simulations. These findings demonstrate that thermally activated adhesion can transform unconsolidated granular packs into mechanically stable plugging zones, providing a mechanistic basis for designing high-stability lost circulation control systems in fractured formations.

1. Introduction

In oil and gas drilling, operations are frequently hampered by persistent lost circulation, a critical technical and economic bottleneck (Zhao et al., 2017; Elkatatny et al., 2020; Wu et al., 2024). Joint assessments by the International Energy Agency and the Society of Petroleum Engineers estimate that global direct economic losses attributed to lost circulation exceed $3 billion annually. Notably, losses occurring in fractured formations account for approximately 60-70% of this total (Abdelaziz et al., 2023; Zang et al., 2025). As drilling targets extend into deeper and more geologically complex settings, conventional bridging lost circulation materials (LCMs) often fail to form a stable plugging zone within fractures (Wang et al., 2020; Blunt et al., 2025).

Lost circulation control in fractured formations presents

Yandy Scientific Press

*Corresponding author.
E-mail address: 15690579183@163.com (Y. Lang); smart-byron@163.com (Y. Bai); sunjsdri@cnpc.com.cn (J. Sun); huazhou@ualberta.ca (H. Li); yangjingbin@upc.edu.cn (J. Yang); lkh54321@126.com (K. Lv).

Received November 20, 2025; revised December 25, 2025; accepted January 19, 2026; available online January 23, 2026.

unique challenges because fractures serve as high-conductivity conduits for drilling fluids, and conventional bridging LCMs often cannot form a high-strength plugging zone (Wang et al., 2023; Zhu et al., 2023). The traditional plugging mechanism relies on granular bridging and accumulation to mechanically obstruct flow (Nguyen et al., 2022). However, these unconsolidated granular packs are mechanically vulnerable to wellbore pressure surges and hydrodynamic erosion caused by formation fluids. Such disturbances frequently destabilize the plugging zone and trigger renewed fluid loss. As a result, remedial treatments in fractured intervals continue to exhibit a low success rate (Feng and Gray, 2018; Bao et al., 2025; Han et al., 2025).

Bridging-material design has evolved from single-phase inert solids to multicomponent composites to improve plugging zone integrity under dynamic downhole conditions. In this framework, rigid particles act as the structural skeleton to resist fracture closure stress (Su et al., 2019; Akbar et al., 2023), elastomeric particles are incorporated to accommodate irregular fracture geometries through deformation, and fibrous materials facilitate network interweaving to improve resistance to hydrodynamic erosion and maintain structural continuity (Bai et al., 2024). As drilling advances into deep and ultra-deep targets, high temperature/high pressure conditions further require thermally robust plugging materials (Pu et al., 2022), including thermosetting resin systems engineered to enhance compressive strength and maintain structural integrity (Wang et al., 2026). Beyond material formulation, adaptive strategies addressing dynamic fracture aperture variations in stress-sensitive reservoirs and complex carbonate environments have been investigated. These include analyses of governing parameters for plugging efficiency, the development of stimuli-responsive LCMs, and numerical modeling of bridging mechanics (Zhao et al., 2021; Wang et al., 2022; Guo et al., 2024). Although these approaches have improved macroscopic plugging performance, the interaction mechanisms among distinct material phases inside fractures remain insufficiently resolved, particularly regarding how multiphase contacts reorganize load transfer and the internal force chain. This gap limits mechanistically guided design of LCM systems and constrains the optimization of component synergy in field applications.

In response to these challenges, thermosensitive adhesive resins (TSARs) emerge as a viable solution to convert unconsolidated granular packs into a coherent, mechanically robust plugging zone. TSARs remain solid under surface conditions, which supports storage, handling, and pumping, but they soften into a viscoelastic state at downhole temperatures. This thermal transition enables adhesive bonding among bridging particles and between particles and fracture walls, increasing cohesion within the plugging zone. Mechanistically, the dominant contact behavior shifts from a friction-dominated regime to an adhesion-mediated regime, which strengthens the particle assembly and improves resistance to hydrodynamic erosion and cyclic pressure loading. Although recent studies on thermally activated adhesive materials report enhanced plugging performance and adaptive functions such as self-healing and broad temperature adaptability (Lei et al., 2022; Yang et al., 2023; Guo et al., 2025), the current evidence base remains largely descriptive at the macroscopic performance level. A key gap persists in micromechanical characterization of stability enhancement, particularly the interfacial compatibility between resin melt viscoelasticity and particle attributes, and the resulting evolution of internal stress transmission and force chain topology.

In the present study, rheological characterization is conducted to quantify the temperature-dependent viscoelastic strength of adhesive composites comprising ethylene-vinyl acetate (EVA) copolymer and representative bridging materials, including quartz sand, calcite, walnut shell, and rubber. Concurrently, photoelastic visualization in a wedge-shaped fracture analogue elucidates the evolution of mesoscale force chain networks under varying loading conditions. Furthermore, discrete element method (DEM) simulations incorporating a linear parallel bond model (LPBM) investigate particle-scale adhesive interactions and link macroscopic material viscoelasticity to mesoscopic contact-network stability. By integrating the experimental and numerical evidence, this work clarifies the synergistic mechanisms by which TSARs and the bridging material type jointly enhance the mechanical stability of the plugging zone in fractures.

2. Experimental section

2.1 Experimental material

To elucidate the mechanisms governing TSAR-bridging material interactions, rheological characterization was performed on composite systems in which 150-180 mesh EVA copolymer was blended with 100-120 mesh bridging agents, including quartz sand, calcite, walnut shell particles, and rubber. For the mesoscopic visualization experiments, polymethyl methacrylate (PMMA), polycarbonate (PC), and polyvinyl chloride (PVC) were selected as photoelastic surrogates to represent different classes of rigid bridging particles. Concurrently, three commercial adhesives (Resin Adhesive-1, Resin Adhesive-2, and Resin Adhesive-3) were used to simulate the viscoelastic behavior of molten TSARs at elevated temperatures; Table 1 lists their chemical compositions and key physicochemical characteristics.

A constitutive mapping was established between the photoelastic analogues (PMMA, PC, and PVC) and field-grade bridging materials (quartz sand, calcite, walnut shell particles, and rubber) to enable a mechanistic interpretation of the surrogate experiments. This comparison focused on key mechanical parameters, specifically elastic modulus (E), Poisson's ratio (ν), interfacial friction coefficients (μ), and the coefficient of thermal expansion (CTE, α). The relevant physicochemical properties and the selection rationale were summarized in Table 2. The photoelastic experiments were conducted at ambient temperature and therefore did not reproduce the thermos-viscoelastic phase transitions of EVA-based TSAR at elevated temperatures, including melting, flow, and re-solidification. Accordingly, the photoelastic analysis was intended to elucidate mesoscale force chain topology and structural stability trends, rather than to directly quantify absolute pressure-bearing capacity under downhole conditions.

Table 1. Chemical compositions and physicochemical characteristics of the resin adhesives.

Resin code	Chemical basis	Physical characteristics	Role in plugging application
Adhesive-1	Polysiloxane-based silicone rubber	High viscoelasticity, flexibility, and resilience; possesses excellent thermal and chemical stability (Baldan, 2012).	Functions as an elastic buffer to provide flexible support, simulating a plugging zone with high deformability.
Adhesive-2	Modified epoxy prepolymer	Characterized by strong interfacial adhesion, high mechanical strength, and viscoelastic behavior (Wei et al., 2020).	Establishes a rigid structural skeleton and robust adhesive, simulating a plugging zone with high pressure-bearing capacity.
Adhesive-3	Ethyl α-cyanoacrylate (instant adhesive)	Features low initial viscosity, ultra-fast curing kinetics, and high post-cure mechanical strength (Maggiore et al., 2021).	Simulates the extreme scenario of instantaneous reaction kinetics and rapid development of high shear strength.

Table 2. Physicomechanical and thermal properties of the photoelastic surrogates and target bridging materials.

Material	Particle classification	E (GPa)	ν (-)	α ($\times 10^{-6}$ K^{-1})	μ (-)
PMMA	Photoelastic	3.1-3.3	0.35-0.40	90-110	~0.54
PC	Photoelastic	2.2-2.4	~0.3	75-80	~0.3
PVC	Photoelastic	2.7-3.0	~0.32	60-80	~0.4
Quartz sand	Bridging	~95.6	~0.084	~3.8	~0.6
Calcite	Bridging	72.3-88.1	~0.31	5.8	/
Walnut shell	Bridging	~0.18	~0.38	~12.3	~0.70
Rubber	Bridging	0.001-0.005	~0.49	180-260	~1.16

2.2 Experimental instruments

The experimental setup comprised an LLH 150 photoelastic polariscope integrated with a custom-designed loading system to simulate fracture plugging conditions, as presented in Fig. 1. This apparatus enabled visual characterization of mesomechanical behavior within the plugging zone during lost circulation control. The approach is based on stress-induced birefringence. When a structural model fabricated from optically active transparent materials is loaded in a polarized light field, isochromatic interference fringes are generated. These fringe patterns were used to interpret internal stress distributions and the evolution of the force chain network.

2.3 Experimental methods

2.3.1 Analysis of interparticle adhesive strength

The temperature-dependent viscoelastic evolution of composite systems formed by TSAR and various bridging materials was characterized using oscillatory temperature sweep tests on a HAAKE Mars60 rheometer. The testing conditions were standardized. The strain amplitude was fixed at 6% to ensure all measurements remained within the linear viscoelastic region (LVR) of the composites. The temperature was ramped from 60 to 120 °C at a heating rate of 2.5 °C/min. This range and heating rate were selected based on differential scanning calorimetry (DSC) of EVA to cover the effective adhesion window. The normal force was maintained at 0.5 N. Measurements were conducted using a cone-plate geometry with a 25 mm diameter and a 0.8 mm gap. The dispersed phase consisted of calcite, quartz sand, walnut shell particles, and rubber, which had a particle size distribution of 100 to 120 mesh and was selected to match the instrument gap and to reduce geometric confinement effects. The continuous phase comprised 150 to 180 mesh EVA particles, which served as the adhesive matrix.

2.3.2 Photoelastic visualization analysis

A custom photoelastic apparatus simulated mesomechanical interactions between TSAR and bridging materials. Conventional bridging agents are optically opaque, and photoelastic measurements at elevated temperatures are technically constrained. Therefore, rigid photoelastic surrogates were adopted to represent bridging particles (Chang et al., 2008; Yan et al., 2021). Specific commercial adhesives were selected to simulate the rheological behavior of molten resin. Isochromatic fringe patterns within the particle assembly were recorded under different loads, and the images were processed in ImageJ to quantify the force chain network. The mechanical interaction effects were evaluated using the following indicators:

1) Average gray value (G^2): The mean gray value of the processed images is used as a proxy for the overall intensity of the force chain network and is taken to reflect

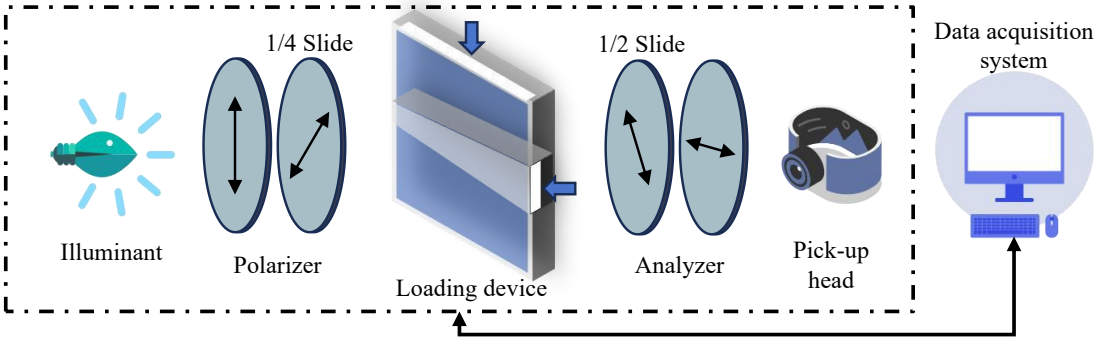

Fig. 1. Schematic representation of the integrated photoelastic visualization apparatus and fracture plugging simulation loading system.

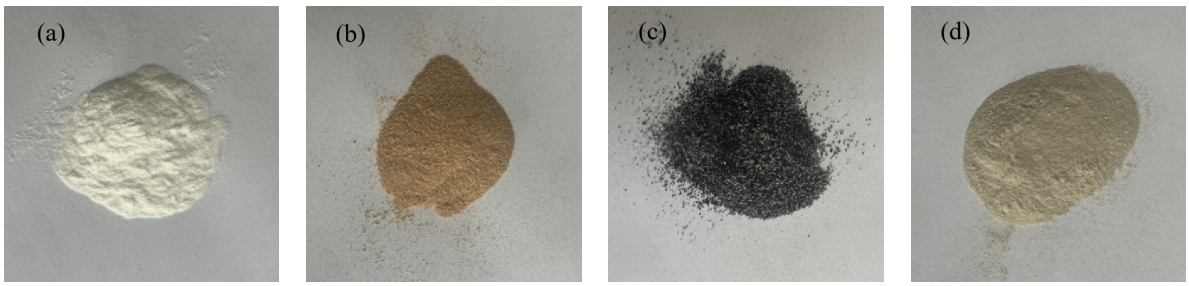

Fig. 2. Macroscopic appearance of the TSAR-bridging material composite blends prepared at a 7:3 volumetric ratio: (a) EVA + calcite, (b) EVA + walnut shell, (c) EVA + rubber and (d) EVA + quartz sand.

the pressure-bearing capacity of the plugging zone.

2) Kurtosis (K): This metric quantifies the peakedness of the gray-value distribution relative to a normal distribution, where excess K equals zero. K greater than 3 indicates stress localization, corresponding to force chain concentration, whereas K less than 3 suggests a flatter distribution associated with a more homogeneous stress field. This metric assesses the stability and uniformity of the force chain network.
3) Proportion of strong force chains (F_p): The grayscale histogram is treated as a bimodal distribution consisting of the force chain foreground and the background. The maximum entropy thresholding method is applied to determine an optimal segmentation threshold (Li et al., 2018). The proportion of pixels with gray values exceeding this threshold is defined as the density of strong force chains and serves as an indicator of contact efficiency and structural stability of the plugging zone.

3. Rheological characterization of TSAR-bridging material composites

3.1 Effect of TSAR dosage on elastic strength

Composite mixtures were prepared by dry blending 100-120 mesh calcite, quartz sand, walnut shell, or rubber with 150-180 mesh EVA. The bridging-material-to-EVA volumetric ratios were set to 5:5, 6:4, 7:3, 8:2, and 9:1, and a resin-free blend served as the control. Figure 2 outlines the formulation scheme used to evaluate the mechanical response of TSAR-bridging-material systems. The temperature-dependent viscoelastic response of each formulation was measured using oscillatory temperature sweeps on a HAAKE Mars60 rheometer. The analysis focused on the storage modulus (G'), which serves as an indicator of elastic resistance. This metric is directly relevant to the mechanical stability of the thermally activated plugging zone under stress loading and pressure transients (Kumar et al., 2018; Hu et al., 2025).

The experimental results are presented in Fig. 3. The thermal evolution of G' shows two regimes. In the low-temperature interval of 60-80 °C, the elastic stiffness increases gradually. In the medium-to-high-temperature interval of 80-120 °C, the stiffness increases rapidly. Compared with the resin-free control, all composite systems exhibit higher G' across the tested TSAR dosages. This trend indicates that thermal activation converts the unconsolidated granular pack into a cohesive, adhesion-strengthened composite (Kishi et al., 2005; Wu et al., 2022). In general, increasing the TSAR volume fraction increases G'. However, at elevated temperatures, formulations with high TSAR content display a nonmonotonic response, where G' increases initially and then decreases, consistent with a loss of elastic stiffness as the resin approaches a flow-dominated state. Across the tested conditions, the elastic stiffness of the EVA composites follows the order: Quartz sand > calcite > rubber > walnut shell particles.

3.2 Effect of TSAR dosage on viscous strength

The variations in the loss modulus (G'') of the resin-particle composites under varying volumetric ratios are presented

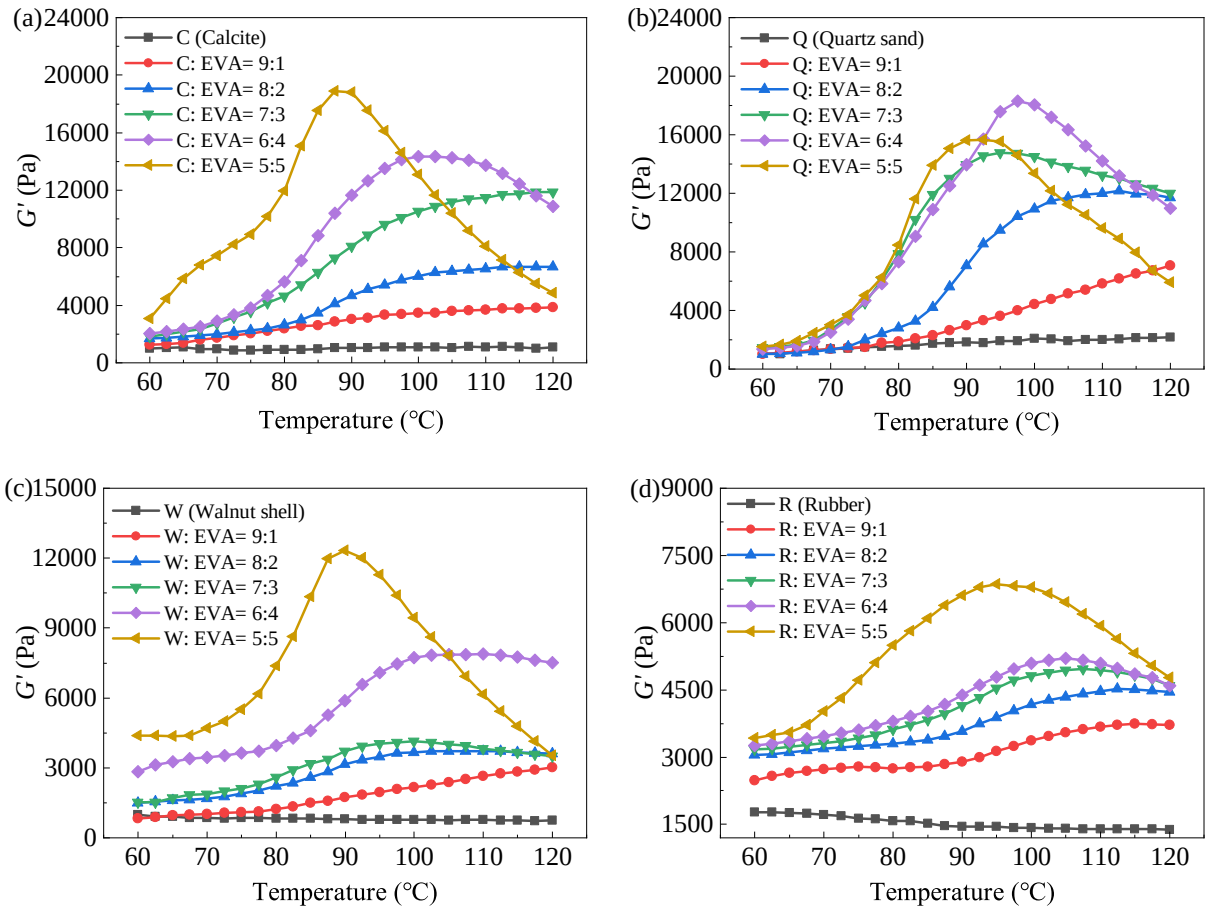

Fig. 3. Elastic properties for composite systems comprising EVA and distinct bridging materials at varying volumetric ratios: (a) Calcite-EVA, (b) quartz sand-EVA, (c) walnut shell-EVA and (d) rubber-EVA.

(Fig. 4). Consistent with the elastic response mechanism, the composites exhibit a characteristic rheological profile. The viscous modulus increases gradually in the low temperature regime of 60-80 °C and accelerates rapidly in the medium to high temperature range of 80-120 °C. After TSAR is incorporated, the loss modulus of all composite formulations increases significantly relative to the resin-free control, indicating enhanced energy dissipation. In general, G'' increases with TSAR volume fraction. However, a deviation is observed in the quartz sand and EVA system, where the viscous component diminishes when the resin volume fraction reaches 50%. Furthermore, at high TSAR loadings, the loss modulus shows a nonmonotonic temperature dependence, increasing initially and then declining, indicating attenuation of viscous properties as the resin approaches its flow point at elevated temperatures. Across the tested systems, the viscous modulus follows the order: Quartz sand > calcite > walnut shell particles > rubber.

Based on the comprehensive analysis of rheological performance across different bridging material types, the optimal bridging-material-to-EVA volumetric ratios are determined as follows: calcite, 6:4; quartz sand, 7:3; walnut shell particles, 6:4; and rubber, 5:5. Among these, the quartz sand and EVA composite demonstrate the most favorable viscoelastic properties, followed by calcite, walnut shell particles, and rubber. This ranking is consistently reflected by the measured viscoelastic indicators, indicating that the composite response depends on both particle stiffness and thermos-mechanical compatibility between the resin phase and the particulate skeleton. This performance hierarchy is primarily governed by the interplay between particle rigidity and CTE. Quartz sand is characterized by high mechanical rigidity and the lowest CTE among the tested materials. Consequently, as temperature increases, quartz particles maintain dimensional stability, thereby minimizing disruptive thermal strain within the adhesive system and preserving the structural integrity of the load-bearing skeleton. In addition, strong physical adsorption and mechanical interlocking between angular quartz surfaces and the EVA matrix likely contribute to stronger interfacial coupling at elevated temperatures, which enhances the overall viscoelasticity of the composite (Zeng et al., 2024). By contrast, rubber particles function as high CTE elastomers. When compounded with resin, the large thermal expansion mismatch and low particle stiffness may hinder the formation of a stable, rigid stress transfer network, resulting in reduced pressure-bearing capacity at the interface (Gao et al., 2024). In summary, the viscoelastic stability of TSAR and bridging material composites is positively correlated with the mechanical rigidity of the bridging particles and negatively correlated

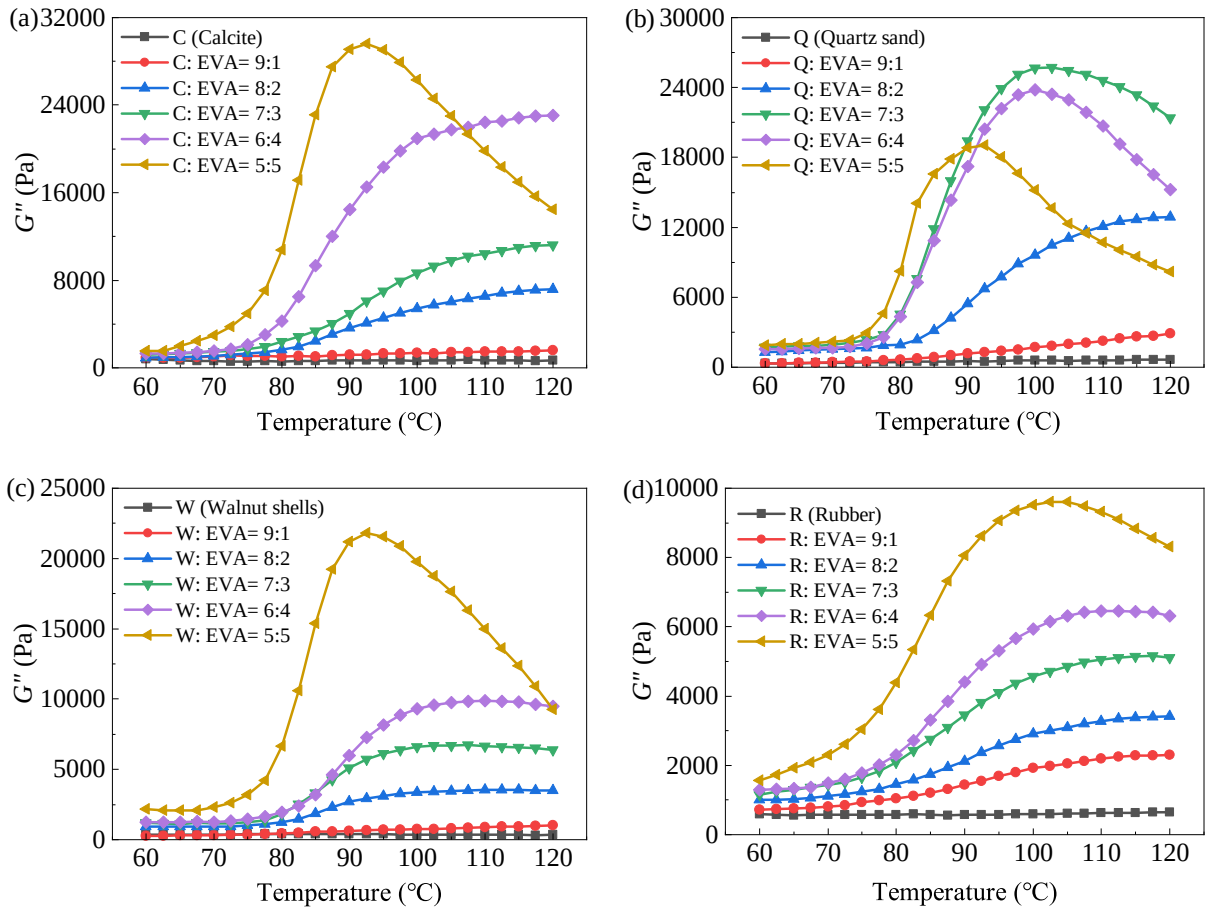

Fig. 4. Viscous properties for composite systems comprising EVA and distinct bridging materials at varying volumetric ratios: (a) Calcite-EVA, (b) quartz sand-EVA, (c) walnut shell-EVA and (d) rubber-EVA.

with their coefficient of thermal expansion.

4. Photoelastic analysis of TSAR effects on force chain evolution in bridging materials

4.1 Selection of an adhesive surrogate for molten TSAR

To identify an optimal adhesive surrogate, a baseline configuration was established using monodisperse PMMA discs with a diameter of 8 mm and a thickness of 3 mm. Experimental configurations were then prepared by uniformly coating the particle periphery with three commercial adhesives, Resin Adhesive-1, Resin Adhesive-2, and Resin Adhesive-3. The evolution of the force chain network was characterized via photoelastic visualization, and the fringe patterns together with the corresponding quantitative indices were integrated to select the optimal surrogate material.

4.1.1 Baseline case: Force chain evolution in monodisperse PMMA

The structural evolution of force chains within the monodisperse PMMA assembly exhibits a characteristic multi-stage response, as illustrated in Fig. S1. In the unloaded state (Fig. S1(a)), the internal stress distribution is uniform, and no discernible force chain network is observed, indicating mechanical equilibrium. After a 30 kg vertical load is applied, a localized force chain network initiates beneath the loading point and propagates along the vertical axis. Consistent with contact mechanics theory, this localized loading induces stress concentration at interparticle contacts, which manifests as the nucleation of vertical force chains as shown in Fig. S1(b) (Li et al., 2018). Subsequently, as the horizontal load is incrementally increased from 10 to 80 kg (Figs. S1(c)-S1(f)), the contact density within the granular assembly rises, enhancing the efficiency of stress transmission. Consequently, a horizontal force chain network progressively develops and becomes the dominant load-bearing structure. Concurrently, the initial vertical force chain network undergoes compression and distortion, leading to tighter interparticle compaction and stress redistribution in the vertical plane (Wang et al., 2016).

As depicted in Fig. 5 and summarized in Table 3, the force chain topology evolves quantitatively during pressurization. Following the initial vertical loading, the stress field exhibits a leptokurtic distribution, indicating that stress is channeled through a limited number of load paths, rendering the network susceptible to instability. As horizontal loading intensifies, the G^2 and the F_p increase, while kurtosis declines. These trends

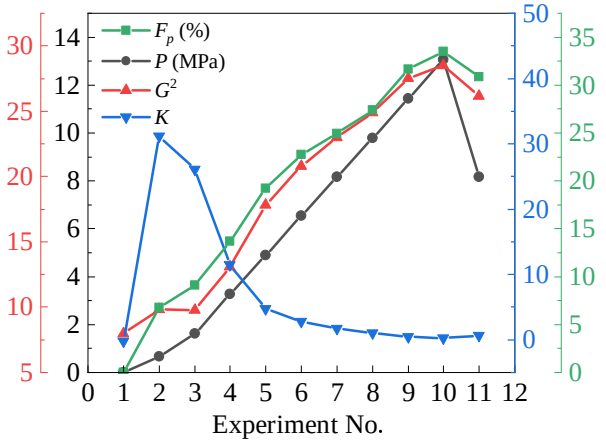

Fig. 5. Quantitative evolution of force chain topology indices for the monodisperse PMMA control assembly under progressive horizontal loading.

Table 3. Force chain characteristics under different pressure conditions.

No.	P (kg)	C_p (MPa)	G^2 (-)	K (-)	F_p (%)
1	0	0.00	7.96	-0.24	0.00
2	V 30	0.67	9.83	31.17	6.77
3	H 10	1.63	9.79	26.14	9.08
4	H 20	3.27	13.08	11.50	13.73
5	H 30	4.90	17.80	4.75	19.23
6	H 40	6.53	20.80	2.82	22.76
7	H 50	8.17	22.97	1.71	24.92
8	H 60	9.80	24.89	1.07	27.42
9	H 70	11.43	27.52	0.42	31.67
10	H 80	13.07	28.48	0.23	33.51
11	Limit	9.80	26.18	0.63	30.84

Notes: P denotes pressure; C_p denotes converted pressure; V denotes vertical; H denotes horizontal.

collectively indicate that the load-bearing network becomes denser, more homogeneous, and structurally robust. At a horizontal load of 80 kg, the system achieves a maximum equivalent plugging pressure of 13.07 MPa, coinciding with the highest F_p and minimal K, which signifies an optimal load-sharing configuration. Beyond this threshold, the trends in G^2, K, and F_p exhibit a critical inflection point. This reversal signals that the primary bridging skeleton destabilizes, causing the structure to collapse and reorganize into a metastable configuration with reduced mechanical integrity.

4.1.2 Experimental group: Monodisperse PMMA with Resin Adhesive-1

The evolution of isochromatic fringe patterns for the PMMA system modified with Resin Adhesive-1 is presented in Fig. S2. In the initial unloaded state, the assembly exhibits

Table 4. Force chain characteristics under different pressure conditions after adding Resin Adhesive-1.

No.	P (kg)	C_p (MPa)	G^2 (-)	K (-)	F_p (%)
1	0	0.00	7.13	-0.74	0.01
2	V 30	0.67	8.26	4.70	5.70
3	H 10	1.63	8.58	7.92	10.72
4	H 20	3.27	12.32	19.06	11.56
5	Limit	1.63	7.42	4.34	4.94

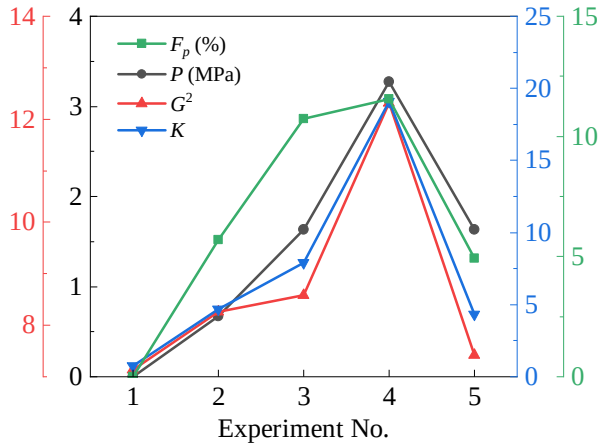

Fig. 6. Quantitative evolution of force chain topology indices for the monodisperse PMMA assembly modified with Resin Adhesive-1 under progressive horizontal loading.

a relatively uniform stress distribution. However, after a 30 kg vertical load is applied, the force chain network distorts markedly and evolves into a tortuous, buckled vertical path. This pattern indicates strong stress localization and the absence of a distributed load sharing skeleton. As horizontal loading increases, incipient horizontal force chain segments appear but fail to merge into a stable, continuous framework. Instead, the bridging structure degrades rapidly, and macroscopic particle slip occurs. This instability suggests that Resin Adhesive-1 modifies the surface tribology of the PMMA particles, thereby reducing both interparticle friction and particle wall friction. Consequently, this adhesive behaves primarily as a lubricant, which impedes rather than promotes the formation of a robust plugging zone.

The quantitative analysis of the force chain evolution is summarized in Table 4 and Fig. 6. The system achieves a maximum equivalent plugging pressure of 3.27 MPa at a horizontal load of 20 kg. At this threshold, the G^2 peaks, and the F_p reaches its maximum, whereas K remains high. This combination implies that the load is carried by a sparse, highly concentrated network with limited redundancy. Consistent with the slip observed in Fig. S2, the abrupt inflection of the quantitative indices beyond the 20 kg load indicates catastrophic failure of the primary force chain skeleton. The assembly is unable to maintain a stable bridging configuration under further pressurization, which leads to structural collapse.

Table 5. Force chain characteristics under different pressure conditions after adding Resin Adhesive-2.

No.	P (kg)	C_p (MPa)	G^2 (-)	K (-)	F_p (%)
1	0	0.00	9.04	26.63	1.87 (bubble)
2	V 30	0.67	13.09	8.89	12.09
3	H 10	1.63	13.25	9.66	11.91
4	H 20	3.27	13.52	9.24	12.64
5	H 30	4.90	14.65	7.51	15.07
6	H 40	6.53	16.18	5.60	19.14
7	H 50	8.17	17.26	3.70	21.49
8	H 60	9.80	18.61	2.57	24.23
9	H 70	11.43	20.83	1.81	26.64
10	H 80	13.07	22.70	1.50	28.59
11	H 90	14.70	23.44	1.35	29.08

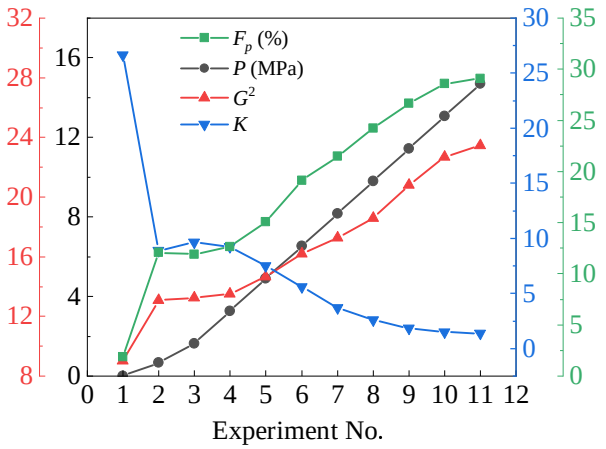

Fig. 7. Quantitative evolution of force chain topology indices for the monodisperse PMMA assembly modified with Resin Adhesive-2 under progressive horizontal loading.

4.1.3 Experimental group: Monodisperse PMMA with Resin Adhesive-2

The photoelastic response of the PMMA assembly modified with Resin Adhesive-2 under varying loads is depicted in Fig. S3. Compared with the control and Resin Adhesive-1 scenarios, Resin Adhesive-2 enhances the mechanical stability of the granular assembly under compression, effectively mitigating macroscopic particle slip. The resulting force chain network is characterized by higher density and improved homogeneity relative to the control group. Serrated fringes emerge and the force chain field becomes more uniformly distributed, suggesting that the interfacial layer undergoes load-dependent deformation rather than remaining mechanically inactive. The serrated fringe patterns, attributed to the intrinsic photoelasticity of the adhesive layer, indicate that the resin phase actively participates in load transmission and facilitates stress redistribution within the composite particulate assembly. This behavior is consistent with a viscoelastic interface capable of accommodating deformation and maintaining stable stress transfer pathways during horizontal compression (Kyriazis et al., 2021).

The force chain evolution in the PMMA + Resin Adhesive-2 system is summarized (Table 5, Fig. 7). The system demonstrates a superior maximum equivalent plugging pressure of 14.70 MPa at a horizontal load of 90 kg. At this peak load, the G^2 and the F_p reach their respective maxima, while the K is minimized. This convergence of indicators suggests the formation of a high-strength, structurally stable plugging zone characterized by a uniform stress distribution. The consistency of these quantitative trends confirms that Resin Adhesive-2 facilitates robust load sharing through a resilient strong-chain skeleton, plausibly associated with its viscoelastic deformation and stress redistribution capability, as observed in Fig. S3. These results indicate that the interfacial coupling between Resin Adhesive-2 and PMMA remains robust under the tested loading conditions. This robustness enables effective stress transfer and dissipation and mitigates localized stress concentrations that may trigger plugging failure.

4.1.4 Experimental group: Monodisperse PMMA with Resin Adhesive-3

Resin Adhesive-3 is uniformly applied to the periphery of the 8 mm PMMA photoelastic discs. On contact with the particle surfaces, the adhesive cures and rigidifies rapidly. Consequently, the resulting interface exhibits brittle fracture characteristics and fails to replicate the viscoelastic behavior required to simulate TSARs in their high-temperature molten state. In addition, the excessive rigidity of the cured system results in permanent adhesion, which renders the adhered PMMA assembly incompatible with the experimental molding apparatus. Based on the comparative analysis of the three adhesive systems, Resin Adhesive-2 demonstrates superior viscoelasticity and a clear capability to enhance the equivalent plugging pressure and structural stability of the plugging zone. Consequently, Resin Adhesive-2 is selected as the optimal photoelastic surrogate to simulate the *in situ* rheological behavior of molten TSARs under high-temperature conditions for the remainder of this study.

4.2 TSAR effects on force chain evolution across photoelastic material types

The evolution of force chain topology across different photoelastic surrogates (PMMA, PC, and PVC) under varying load conditions is depicted in Fig. S4. After the initial 30 kg vertical load is applied, the primary force chain network in all resin-free assemblies exhibits a distinct vertical orientation. As horizontal loading increases, localized stress concentrations emerge within the PMMA and PVC assemblies, which facilitate the formation of high-strength bridging structures. Comparative analysis indicates that the equivalent plugging pressure capacity of PMMA and PVC surrogates is superior to that of PC. However, the PVC assembly exhibits significant compressive deformation and macroscopic slip at the fracture tip during horizontal pressurization, which indicates that its

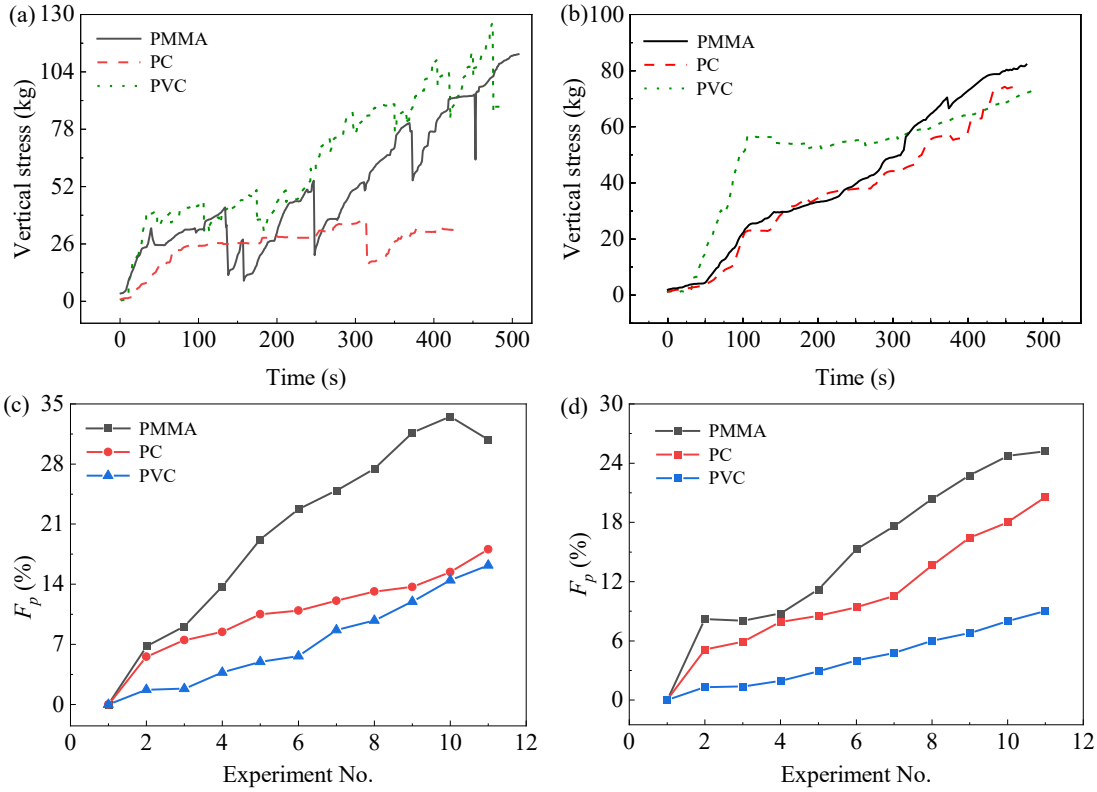

Fig. 8. Effects of TSAR on force chain evolution during pressurization across different photoelastic material types: Vertical stress variation for (a) single-material assemblies and (b) adhesive composites; F_p for (c) single-material assemblies and (d) adhesive composites.

frictional characteristics and mechanical stability are suboptimal for this application. The structural evolution of the force chain network in the TSAR composite systems is depicted (Fig. S5). Under the initial 30 kg vertical load, the primary force chain retains a predominantly vertical distribution. Compared with the resin-free controls, the composites show lower peak stress intensities and fewer isolated high-stress chains. As horizontal load increases, the force chain network in all composite systems expands laterally, indicating more uniform propagation. Although the peak stress intensity of the main force chain is reduced relative to the rigid controls, the total number of particles participating in the load-bearing skeleton increases significantly. This shift supports a transition from localized, high-intensity bridging to a distributed, cooperative load-bearing mechanism. The reduction in main chain intensity coupled with the increased fraction of particles incorporated into the load-bearing skeleton improves network uniformity and global stability (Nina et al., 2020).

The impact of TSAR on vertical-stress evolution and the F_p across different photoelastic materials during pressurization is shown in Fig. 8. The incorporation of Resin Adhesive-2 effectively attenuates the fluctuations in vertical stress typically observed during horizontal loading and reduces the absolute magnitude of vertical stress transmission at equivalent horizontal loads. Furthermore, as pressure increases, the resin stabilizes the rate of strong force chain formation. These quantitative trends indicate that Resin Adhesive-2 possesses strong viscoelasticity and stress-redistribution capability. Under compressive loading, the resin phase accommodates deformation and dissipates locally concentrated stresses over a larger interfacial area. This mechanism homogenizes the force chain network and enhances the overall mechanical integrity and stability of the plugging zone.

4.3 TSAR effects on force chain evolution across particle sizes

The evolution of force chain topology within assemblies of varying particle sizes (5, 8, 10 mm, and polydisperse mixtures) under progressive loading is illustrated in Fig. S6. Across all particle diameters, the force chain network becomes increasingly complex as pressurization progresses, and local stress concentrations intensify. Clear size-dependent responses are observed. The fine-grained assembly (5 mm) progressively develops a compact and ordered force chain network. By contrast, the coarse-grained assembly (10 mm) and the polydisperse system exhibit more pronounced stress localization and a more heterogeneous force chain orientation. These differences are consistent with coordination-number effects. Smaller particles produce a higher density of contact points, which promote more uniform stress distribution, whereas larger particles, with fewer contact points and greater relative displacement, are more prone to severe stress concentration at contact interfaces. In the polydisperse system, fine particles partially occupy the interstitial voids between coarse particles, alter contact modes,

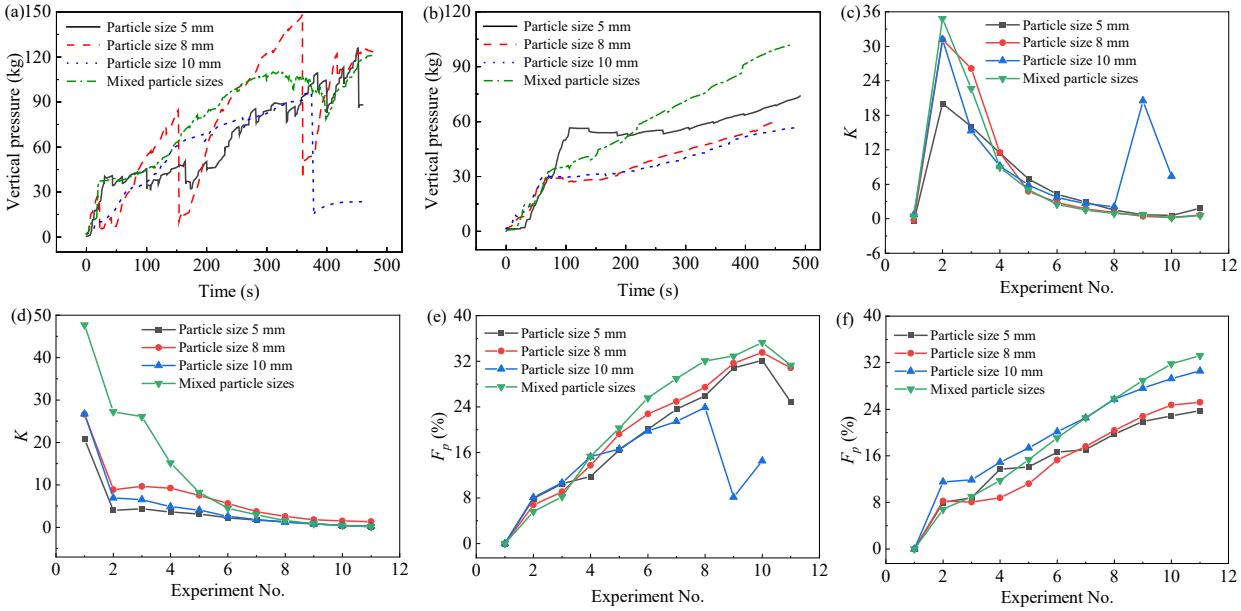

Fig. 9. Effects of TSAR on force chain evolution during pressurization across different particle sizes: Vertical stress variation for (a) single-size assemblies and (b) adhesive composites; K variation for (c) single-size assemblies and (d) adhesive composites; F_p for (e) single-size assemblies and (f) adhesive composites.

and create secondary stress-transfer pathways, which enhance network stability.

The photoelastic response of these assemblies after modification with Resin Adhesive-2 is shown (Fig. S7). The resin-induced enhancement in effective contact area and stress homogenization increases with particle size. For fine-grained assemblies, where the native contact density is already high, the resin provides only marginal additional stress dispersion. As particle size increases, the resin plays a critical role in alleviating the severe stress concentrations intrinsic to coarse-grained packs. By filling interstitial voids and increasing the effective contact area, the resin converts point contacts into area contacts. In the polydisperse system, the resin acts as a viscoelastic bridge, mitigating stiffness mismatch between heterogeneous particles and facilitating more uniform load transfer.

The quantitative evolution of the force chain structure is summarized (Fig. 9). In the absence of resin, fine-grained assemblies exhibit stable vertical stress accumulation under horizontal compression, whereas coarse-grained assemblies display significant pressure fluctuations and reduced bearing capacity. The polydisperse system exhibits the lowest K, suggesting that an optimized particle size distribution (PSD) enhances the structural stability of the plugging zone. Following the incorporation of Resin Adhesive-2, the vertical stress response across all particle sizes stabilizes and is characterized by a steady increase with significantly attenuated fluctuations. Although the absolute magnitude of vertical stress transmission decreases at equivalent horizontal loads, indicating stress relaxation through the viscoelastic matrix, K decreases and becomes more uniform across all groups. In parallel, the evolution of the F_p becomes more stable under increasing load. Together, these trends suggest that the resin prevents catastrophic disruption of the force chain network and enhances the pressure-bearing stability of the plugging zone through improved stress homogenization.

4.4 TSAR effects on force chain structure across particle shapes

The influence of particle shape on force chain network evolution is investigated using PMMA surrogates with varying geometries (rectangular, rhombic, triangular, square, circular, and elliptical), with the results summarized in Fig. 10. In the absence of resin, the vertical stress response exhibits distinct shape-dependent behaviors. Angular particles (rectangular, rhombic, triangular, and square) demonstrate a steady increase in vertical stress with rising horizontal load, which is attributed to mechanical interlocking. Among these, rectangular particles exhibit the most pronounced vertical stress transmission and the highest force chain intensity. Conversely, rounded geometries (circular and elliptical) display significant instability characterized by high-amplitude stress fluctuations due to the lack of interparticle locking. Adding Resin Adhesive-2 fundamentally changes the mechanical response. The rate of vertical stress accumulation is moderated across all morphological groups, and the magnitude of stress fluctuations is significantly attenuated. During the low to intermediate loading stages, stress evolution remains gradual as the viscoelastic resin redistributes within the interstitial void space and dissipates localized stress concentrations. At higher loads, vertical stress increases more linearly and uniformly with horizontal compression. The evolution of K further corroborates this stabilization. For all particle shapes, resin addition results in lower K values at equivalent load levels, indicating a shift from localized, high-intensity force chain to a more homogeneous stress distribution. Concurrently, the rate of strong force chain

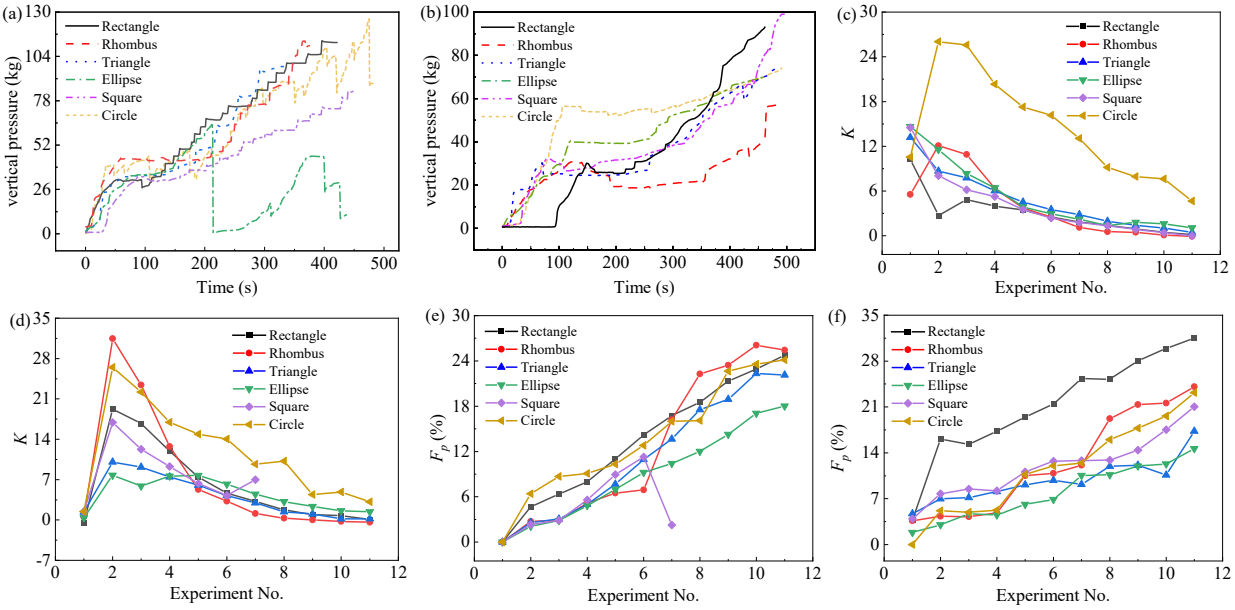

Fig. 10. Effects of TSAR on force chain evolution during pressurization across different particle shapes: Vertical stress variation for (a) single-shape assemblies and (b) adhesive composites; K variation for (c) single-shape assemblies and (d) adhesive composites; F_p for (e) single-shape assemblies and (f) adhesive composites.

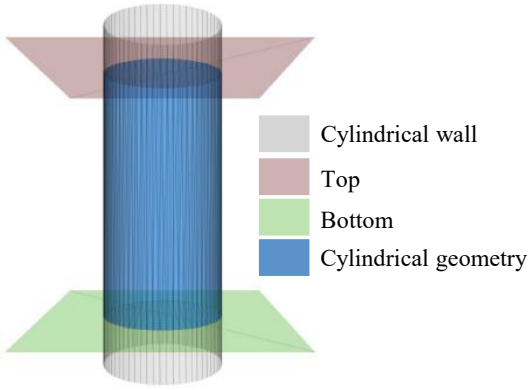

Fig. 11. DEM model geometry of TSAR particles and bridging particles of different types.

formation is modulated. Collectively, these observations indicate that the resin promotes viscoelastic deformation, void filling, and adhesive coupling. As a result, the friction-dominated pack transitions into a cohesive, adhesion-mediated composite, which reduces sensitivity to particle morphology and stabilizes the force chain network.

5. DEM simulation of TSAR interactions with bridging materials

5.1 Model construction and parameter optimization

5.1.1 Assumptions of the model

At elevated formation temperatures, TSARs and bridging materials interact to form a cohesive resin-particle composite. To investigate the micromechanical behavior of these interactions, the DEM was employed using the Particle Flow Code (PFC) software (Mohajeri et al., 2020). PFC facilitated the construction of microstructural models at the particle scale, which enabled the rigorous simulation of stress-strain evolution during the resin adhesive phase. Furthermore, the method accurately captured the contact mechanics, adhesive coupling, and decohesion mechanisms at interparticle interfaces (Kan et al., 2015; Almohammed and Breuer, 2016; Chu et al., 2026). To balance computational cost and physical fidelity, the following simplifying assumptions were imposed on the numerical model:

1) Boundary conditions: The geometric boundaries of the model were defined as ideal rigid walls (Fig. 11); wall compliance and heat exchange between the boundary and the fluid were neglected.
2) Particle morphology: Both the bridging agents and resin-particles were modeled as ideal spheres, as shown in Fig. 12(a), to streamline contact detection.
3) Material homogeneity: The physicochemical properties of the TSAR and bridging materials were assumed to be isotropic and homogeneous at the microscopic scale throughout the contact and adhesive processes.
4) Thermodynamic state: The simulations assumed isothermal conditions; environmental temperature fluctuations were neglected within the simulated timeframe.

5.1.2 Selection of the contact constitutive model

For the numerical investigation of the interaction between TSARs and bridging materials, selecting a constitutive model capable of accurately capturing the temperature-dependent adhesive behavior of resin-particles is critical. LPBM was identified as the optimal constitutive law for describing the cementation mechanics within the composite assembly. Physically, the LPBM establishes a finite-sized bonded interface

Table 6. Calibrated micromechanical parameters for particle contacts in the DEM model at 80 °C.

Sample	E^* (MPa)	k^* (-)	μ (-)	β_n (-)	σ_c (MPa)	c (MPa)	φ (°)
EVA	0.8	5	0.7	0.1	1.5	3.0	25
Quartz sand	60	3.5	0.5	0.075	0	0	30
Calcite	35	3.5	0.6	0.085	0	0	32.5
Rubber	3	2	0.75	0.075	0	0	30
Walnut shell	10	3	0.5	0.035	0	0	27.5

Notes: E^* denotes effective modulus; k^* denotes stiffness ratio; μ denotes friction coefficient; β_n denotes critical damping ratio; σ_c denotes tensile strength; c denotes cohesion; φ denotes friction angle.

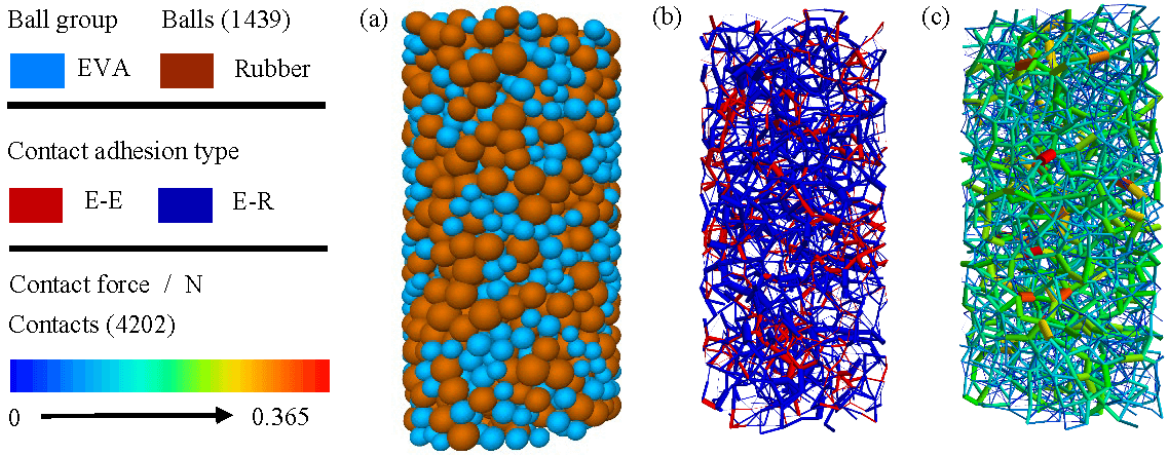

Fig. 12. DEM representation of the EVA-rubber composite: (a) Particle group, (b) adhesion force, and (c) contact force.

at the contact between two particles. Mechanically, the model comprises three components: Linear springs (normal and shear stiffness), dashpots (viscous damping), and a parallel bond. The bond transmits both forces (tension, compression, and shear) and moments (bending and twisting). This formulation provides a rigorous framework for simulating the cohesive and adhesive interactions within the TSAR-bridging material composite system.

5.1.3 Model geometry and parameter calibration

To validate the mesoscopic interaction mechanisms and corroborate the experimental findings, a representative numerical model was constructed. EVA was defined as the thermosensitive adhesive phase (density: 950 kg/m^3), whereas quartz sand, calcite, rubber, and walnut shell were defined as bridging phases (densities: 2600, 2750, 940, and 1100 kg/m^3, respectively). The simulation domain was defined as a cylindrical rigid-wall boundary with a radius of 4 mm and a height of 16 mm. Within this volume, a particle assembly was generated with a target porosity of 0.40 and a fixed EVA-to-bridging-material volumetric ratio of 3:7. The particle size distribution was specified using radius ranges of 0.30-0.425 mm for EVA particles and 0.425-0.60 mm for bridging particles. To ensure simulation accuracy, the micromechanical parameters of the TSAR and bridging materials (Table 6) were calibrated against experimental mechanical data obtained at 80 °C.

Using the EVA-rubber composite system as a representative case, the interparticle contact logic was rigorously defined as follows: Parallel adhesive contact between EVA particles, Hertzian contact between rubber particles, and parallel adhesive contact between rubber and EVA particles. Adhesive interactions between particles and the wall surface were neglected. The relevant mechanical data were ultimately obtained after the model reached a steady state.

5.2 DEM analysis of TSAR interactions with bridging materials

5.2.1 Micromechanical visualization of interparticle stress

The micromechanical interactions within the resin and bridging particle composites are elucidated using the rubber and EVA system as a representative case, as shown in Fig. 12. The spatial configuration at 80 °C is depicted in Fig. 12(a), which illustrates a homogeneous dispersion of EVA particles within the rubber matrix. The topology of the adhesive-bond network is visualized (Fig. 12(b)). Based on the line density and thickness, the intensity and spatial distribution of adhesive interactions can be inferred. The simulation results indicate a total of 2,820 adhesive contacts within the domain, yielding an average coordination number of approximately 4 for the EVA phase. This high degree of connectivity confirms the formation

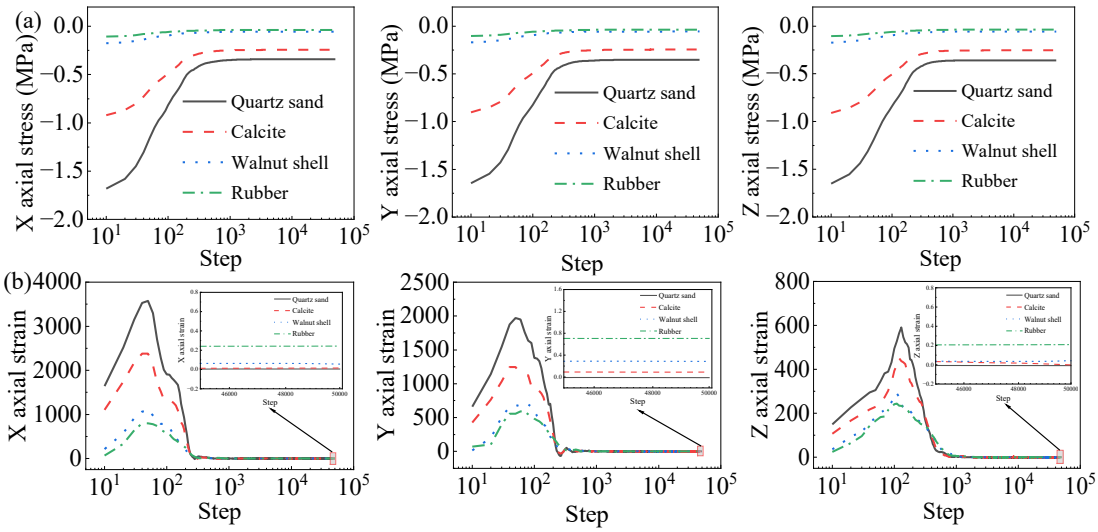

Fig. 13. Triaxial mechanical response during TSAR adhesion to different bridging materials: (a) Axial stress and (b) axial strain.

Table 7. Force parameters between TSAR and different types of bridging materials at 80 °C.

Adhesive type	Number of contacts	Adhesive force (N)	Contact force (N)
EVA + quartz sand	2,807	0-3.51	0-4.71
EVA + calcite	2,806	0-2.33	0-4.21
EVA + walnut shell	2,822	0-0.54	0-0.64
EVA + rubber	2,820	0-0.34	0-0.36

of a complex, reticulated adhesive force chain network (Wang et al., 2023; Fan et al., 2025). The particles within the composite assembly are subjected to a coupled stress state governed by the superposition of adhesive bonding, elastic contact forces, gravitational loading, and frictional interactions. The magnitude of the resultant contact-force vectors on each particle is mapped (Fig. 12(c)). The peak interparticle force recorded is 0.365 N. The color map delineates the heterogeneity of force transmission. Regions with high contact force magnitudes represent zones of stress concentration, which substantially influence the macroscopic mechanical stability of the plugging zone.

The quantitative contact-mechanics metrics for the different bridging-material pairings at 80 °C were extracted from the DEM simulations (Table 7). A comparative analysis reveals a distinct hierarchy in both adhesive bond strength and total contact force magnitude: EVA-quartz sand > EVA-calcite > EVA-walnut shell > EVA-rubber. Crucially, this DEM-derived hierarchy of interparticle adhesion aligns well with the macroscopic rheological characterization presented in Section 3. The consistency across scales suggests that the same particle-level attributes influencing interparticle adhesion also contribute to the bulk viscoelastic response. This agreement provides cross-scale consistency between the mesoscopic numerical simulation and the macroscopic experimental results, and confirms that particle rigidity and surface properties govern the efficiency of the TSAR-mediated adhesive mechanism.

5.2.2 Triaxial stress-strain analysis of resin-particle composites

As depicted in Fig. 13, the triaxial mechanical behavior of the TSAR bridging systems includes axial stress evolution (Fig. 13(a)) and axial strain response (Fig. 13(b)). Regarding the axial stress evolution, the quartz sand and EVA composite exhibit the highest peak stress magnitudes across all loading directions. This response indicates the rapid establishment of a high-stiffness stress transmission network and a robust load-bearing skeleton during the adhesive process. The calcite and EVA composite display intermediate stress levels, suggesting that the interfacial coupling stiffness between calcite and EVA is lower than that of the quartz-based system. Conversely, the walnut shell and EVA composite exhibit substantially lower axial stress values. Stress accumulation in this system is gradual and plateaus at a low magnitude, indicating weak interfacial adhesion and limited stress transmission efficiency under external loading. Similarly, the rubber and EVA composite maintain a consistently low stress profile throughout deformation. This behavior is attributed to the low elastic modulus of the rubber phase and its high mechanical compliance relative to the EVA matrix, which promotes stress relaxation and attenuates stress transfer at the adhesive interface.

Regarding the axial strain behavior, distinct transient fluctuations are observed during the initial simulation phase. These artifacts are attributed to the stochastic particle generation and packing stabilization processes inherent to the PFC algorithm. Consequently, the analysis focuses exclusively on the steady-state strain response following adhesive stabilization. In this regime, the magnitude of axial strain follows the descending order: Rubber > walnut shell > calcite > quartz sand. This hierarchy corroborates a synergistic plugging mechanism that combines rigid bridging and flexible filling to form a stable plugging zone in fractures. Quartz sand, acting as a rigid part-

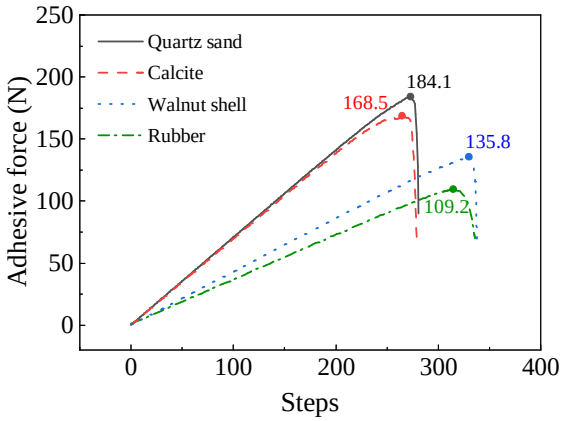

Fig. 14. Numerical simulation results of tensile tests on adhesive composites of TSAR and different types of bridging materials.

iculate, serves as the primary structural bridging component to bear formation stress, whereas rubber, serving as a compliant particulate, deforms to occlude interstitial voids between rigid bridges. When coupled with the thermosensitive adhesive mechanism of the resin, these results provide mechanistic guidance for optimizing TSAR-enhanced lost circulation control systems.

5.2.3 Tensile analysis of resin-particle composites

The tensile failure behavior of the composite systems was investigated via direct tension simulations, which were conducted by applying opposing constant velocity boundary conditions to the upper and lower particle subsets along the Z-axis. As depicted in Fig. 14, the resultant adhesive tensile force for the EVA-based composites with different bridging materials evolves over time. The quartz sand-EVA system and the calcite-EVA system exhibit a rapid escalation in tensile resistance during the initial loading stage. The quartz sand and EVA composite achieve the maximum peak tensile force of approximately 184.1 N. The magnitude of the peak adhesive force across the tested systems follows the descending order: Quartz sand > calcite > walnut shell > rubber. This hierarchy is consistent with the macroscopic viscoelastic characterization results for TSAR and bridging material composites discussed in Section 3. These findings substantiate that the adhesive coupling strength between TSAR and rigid particles was significantly greater than that observed with flexible particles. Moreover, tensile performance is positively correlated with the mechanical rigidity and surface characteristics of the bridging agents, confirming that rigid and angular particles promote stronger interfacial adhesion with the resin matrix.

6. Conclusions

Addressing the critical challenge of insufficient plugging zone stability in fractured formations, this study elucidates the interaction mechanisms between TSARs and four distinct bridging materials, quartz sand, calcite, walnut shell, and rubber. The investigation employs an integrated multiscale methodology comprising rheological characterization, mesoscopic photoelastic visualization, and DEM simulations. The principal conclusions are summarized as follows:

1) The optimal volume ratios of bridging materials to TSAR are determined as follows: Quartz sand: EVA = 7:3, calcite: EVA = 6:4, walnut shell: EVA = 6:4, rubber: EVA = 5:5. Within the 60-120 °C range, the viscoelasticity of the composite system is positively correlated with the hardness of the bridging material and is negatively correlated with the thermal expansion coefficient, and the quartz sand-EVA system exhibits the best performance.
2) Resin Adhesive-2 is selected as the preferred substitute for high-temperature molten resin. It enhances the pressure-bearing capacity (up to a maximum of 14.70 MPa) across bridging materials of different types, particle sizes, and shapes via gap filling, stress dispersion, and force chain optimization.
3) DEM simulations based on the Linear Parallel Bond Model show that the quartz sand-EVA system has the highest adhesive force of 3.51 N and contact force of 4.71 N at 80 °C, along with the highest peak triaxial stress and the smallest strain. This result supports a plugging mechanism combining rigid bridging, flexible filling, and thermosensitive adhesion.

These conclusions are subject to the investigated temperature window (60-120 °C) and the simplifying assumptions inherent to the experimental configurations and numerical model. Consequently, the findings primarily clarify mechanistic trends and relative material hierarchies. Absolute field-scale pressure-containment capacities require further validation under coupled high temperature/high pressure conditions with realistic formation boundary interactions.

Acknowledgements

This research is financially supported by the National Natural Science Foundation of China (No. 52374023), Oil & Gas National Science and Technology Major Project (No. 2025ZD1401903), Deep Earth National Science and Technology Major Project (No. 2024ZD1000905), Taishan Scholar Young Expert (No. tsqn202306117) and the Postdoctoral Fellowship Program of CPSF (No. GZC20251950).

Supplementary file

https://doi.org/10.46690/ager.2026.0x.0x

Conflicts of interest

The authors declare no competing interest.

References

Abdelaziz, A., Ha, J., Li, M., et al. Understanding hydraulic fracture mechanisms: From the laboratory to numerical modelling. Advances in Geo-Energy Research, 2023, 7(1): 66-68.

Akbar, R., Setiati, R., Maulindani, S., et al. Practical approach

solving the lost circulation problem during drilling operation. International Journal of Application on Sciences, Technology and Engineering, 2023, 1(1): 253-259.

Almohammed, N., Breuer, M. Modeling and simulation of particle-wall adhesion of aerosol particles in particle-laden turbulent flows. International Journal of Multiphase Flow, 2016, 85: 142-156.

Bai, Y., Liu, Y., Sun, J., et al. Plugging mechanism of rigid and flexible composite plugging materials for millimeter-scale fractures. SPE Journal, 2024, 29(4): 1786-1801.

Baldan, A. Adhesion phenomena in bonded joints. International Journal of Adhesion and Adhesives, 2012, 38: 95-116.

Bao, D., Liu, S., Yang, Y., et al. Preparation and performance of high temperature resistant and high strength self-healing lost circulation material in drilling industry. Petroleum Science, 2025, 22(9): 3655-3670.

Blunt, M. J., Sun, S., Boone, M. A., et al. Digital rock physics and fluid flow in the context of the energy transition. Advances in Geo-Energy Research, 2025, 18(3): 299-302.

Chang, C., Lien, H., Lin, J. Determination of reflection photoelasticity fringes analysis with digital image-discrete processing. Measurement, 2008, 41(8): 862-869.

Chu, J., Huang, G., Li, M., et al. A CFD-DEM simulation study on the evolution of the plugging layer during the temporary plugging and diverting fracturing. Fuel, 2026, 405: 136688.

Elkatatny, S., Ahmed, A., Abughaban, M., et al. Deep illustration for loss of circulation while drilling. Arabian Journal for Science and Engineering, 2020, 45(2): 483-499.

Fan, Z., Liu, D., Heynderickx, G., et al. Interface-resolved simulation of droplet-particle interaction dynamics in multi-particle collisions. Physics of Fluids, 2025, 37(4): 043334.

Feng, Y., Gray, K. Modeling lost circulation through drilling-induced fractures. SPE Journal, 2018, 23(1): 205-223.

Gao, Z., He, H., Yang, Z., et al. Improved adhesion of rubber composites by developing environmentally friendly fiber impregnation coatings with good interfacial modulus transition gradients. Progress in Organic Coatings, 2024, 189: 108325.

Guo, K., Kang, Y., Lin, C., et al. A novel experimental study on plugging performance of lost circulation materials for pressure-sensitive fracture. Geoenergy Science and Engineering, 2024, 242: 213214.

Guo, K., Kang, Y., Xu, C., et al. Plugging mode of flaky lost circulation materials within fractures and mechanism to enhance pressure-bearing capacity for the plugging zone. Petroleum Science, 2025, 22(8): 3315-3332.

Han, Z., Yang, X., Ren, N., et al. Dynamic sealing mechanisms of drilling fluid in fractured coalbed methane formations: a coupled CFD-DEM numerical study. Computers and Geotechnics, 2025, 188: 107560.

Hu, Z., Zhang, Y., Wang, J., et al. Experimental study of a circulation agent dynamic plugging for multi-scale natural fractures. Petroleum Science, 2025, 22(9): 3641-3654.

Kan, H., Nakamura, H., Watano, S., et al. Numerical simulation of particle-particle adhesion by dynamic liquid bridge. Chemical Engineering Science, 2015, 138: 607-615.

Kishi, H., Uesawa, K., Matsuda, S., et al. Adhesive strength and mechanisms of epoxy resins toughened with preformed thermoplastic polymer particles. Journal of Adhesion Science and Technology, 2005, 19(15): 1277-1290.

Kumar, R., Kar, K., Dasgupta, K., et al. Static and dynamic mechanical analysis of graphite flake filled phenolic-carbon fabric composites and their correlation with interfacial interaction parameters. Polymer Engineering & Science, 2018, 58(11): 1987-1998.

Kyriazis, A., Kilian, R., Sinapius, M., et al. Tensile strength and structure of the interface between a room-curing epoxy resin and thermoplastic films for the purpose of sensor integration. Polymers, 2021, 13(3): 330.

Lei, S., Sun, J., Bai, Y., et al. Plugging performance and mechanism of temperature-responsive adhesive lost circulation material. Journal of Petroleum Science and Engineering, 2022, 217: 110771.

Li, F., Yang, L., Wang, J., et al. A quantitative extraction method of force chains for composite particles in a photoelastic experiment. Chinese Journal of Engineering, 2018, 40(3): 302-312. (in Chinese)

Maggiore, S., Banea, M. D., Stagnaro, P., et al. A review of structural adhesive joints in hybrid joining processes. Polymers, 2021, 13(22): 3961.

Mohajeri, M., Helmons, R., Rhee, C., et al. A hybrid particle-geometric scaling approach for elasto-plastic adhesive DEM contact models. Powder Technology, 2020, 369: 72-87.

Nguyen, K., Mehrabian, A., Bathija, A., et al. Compression of particulate materials in wellbore fractures and enhancement in the wellbore breakdown limit. Journal of Applied Mechanics, 2022, 89(10): 101002.

Nina, L., Marlis, E., Bogna, S. Bond strength between a high-performance thermoplastic and a veneering resin. The Journal of Prosthetic Dentistry, 2020, 124(6): 790-797.

Pu, L., Xu, P., Xu, M., et al. Lost circulation materials for deep and ultra-deep wells: A review. Journal of Petroleum Science and Engineering, 2022, 214: 110404.

Su, X., Lian, Z., Xiong, H., et al. Laboratory study on a new composite plugging material with high bearing strength and high-temperature resistance. Journal of Chemistry, 2019, 2019: 1874617.

Wang, C., Yao, X., Du, T., et al. High-compression-resistant thermosetting resins as plugging materials for oil-based drilling fluids. Recent Patents on Mechanical Engineering, 2026, 19: 1-11.

Wang, G., Huang, Y. Numerical investigation on the fracture-bridging behaviors of irregular non-spherical stiff particulate lost circulation materials in a fractured leakage well section. Geoenergy Science and Engineering, 2023, 223: 211577.

Wang, J., Li, J., Liu, G., et al. Development of a wellbore heat transfer model considering circulation loss. Arabian Journal of Geosciences, 2020, 13(2): 85.

Wang, J., Liang, C., Pang, W. Photoelastic experiment on force chain evolution of particle aggregate under the conditions of biaxially loading and bilaterally flowing. Rock and Soil Mechanics, 2016, 37(11): 3041-3047. (in Chinese)

Wang, X., You, L., Zhu, B., et al. Numerical simulation of bridging ball plugging mechanism in fractured-vuggy carbonate reservoirs. Energies, 2022, 15(19): 7361.

Wei, H., Xia, J., Zhou, W., et al. Adhesion and cohesion of epoxy-based industrial composite coatings. Composites Part B: Engineering, 2020, 193: 108035.

Wu, H., Li, G., Xu, G., et al. Emulsion properties and plugging performances of active crude oil enhanced by amphiphilic Janus nanosheets. Petroleum Science, 2024, 21(6): 4141-4152.

Wu, J., Li, C., Hailatihan, B., et al. Effect of the addition of thermoplastic resin and composite on mechanical and thermal properties of epoxy resin. Polymers, 2022, 14(6): 1087.

Xu, C., Zhong, J., Luo, S., et al. Mechanism and material development of temperature activated bonding plugging for lost circulation control in deep fractured formations. SPE Journal, 2025, 30(10): 6097-6111.

Yan, X., Huo, B., Deng, S., et al. Clarify the effect of fracture propagation on force chains evolution of plugging zone in deep fractured tight gas reservoir based on photoelastic experiment. Geoenergy Science and Engineering, 2024, 233: 212558.

Yan, X., Xu, C., Kang, Y., et al. Mechanical mechanism of meso-structure instability of fracture plugging zone based on the characterization of force chain network. Acta Petrolei Sinica, 2021, 42(6): 765-775. (in Chinese)

Yan, X., Xu, C., Kang, Y., et al. Mesoscopic structure characterization of plugging zone for lost circulation control in fractured reservoirs based on photoelastic experiment. Journal of Natural Gas Science and Engineering, 2020, 79: 103339.

Yang, L., Ma, J., Chang, X., et al. Novel polymeric organic gelator as lost circulation material for oil-based drilling fluids. Geoenergy Science and Engineering, 2023, 231: 212414.

Yao, X., Jian, L., Xu, W., et al. Digital shifting photoelasticity with optical enlarged unwrapping technology for local stress measurement. Optics & Laser Technology, 2005, 37(7): 582-589.

Zang, X., Qiu, Z., Jiang, L., et al. Unravelling fracture plugging behavior of granular temporary plugging agents for a sustainable geothermal development. Fuel, 2025, 387: 134351.

Zeng, X., Duanmu, W., Gao, Z., et al. Research on flexible base discrete adhesion model of SCAPW for blade machining. Journal of Manufacturing Processes, 2024, 118: 173-186.

Zhao, P., Santana, C., Feng, Y., et al. Mitigating lost circulation: A numerical assessment of wellbore strengthening. Journal of Petroleum Science and Engineering, 2017, 157: 657-670.

Zhao, S., Zhu, D., Bai, B., et al. Experimental study of degradable preformed particle gel (DPPG) as temporary plugging agent for carbonate reservoir matrix acidizing to improve oil recovery. Journal of Petroleum Science and Engineering, 2021, 205: 108760.

Zhu, N., Ding, S., Shi, X., et al. Numerical analysis of the connector effect on cuttings bed transportation while Tripping. Geoenergy Science and Engineering, 2023, 227: 211817.